Applied Surface Science 509 (2020) 144874

Contents lists available at ScienceDirect

Applied Surface Science

journal homepage: www.elsevier.com/locate/apsusc

Full Length Article

Near-infrared emission from modified zinc oxide hybrid nanostructures

Jung-Soo Kang*, Kam Tong Leung**

Waterloo Advanced Technology Laboratory and Department of Chemistry, University of Waterloo, Waterloo, Ontario N2L 3G1, Canada

ARTICLE INFO

Keywords:
Near-infrared emission
Zinc oxide nanostructures
Surface functionalization
Neodymium
Energy transfer

ABSTRACT

Near-infrared emission is receiving of attention due to its wide range of applications in imaging, optoelectronics and telecommunication. Here, we synthesize rare earth based organic complexes and use them to endow near-infrared emission capability into two-dimensional nanostructured transparent conducting oxide, specifically zinc oxide nanowalls. The hybrid ZnO nanowalls with Nd^{3+} complex are found to successfully generate characteristic near-infrared emissions at 887, 1066 and 1334 nm. X-ray photoelectron spectroscopy and theoretical calculations show that the interfacial interactions between ZnO and the Nd^{3+} complex are driven by nitrate anions in the complex. Based on these results, we propose an unique cascade energy transfer mechanism from ZnO to Nd^{3+} via 1,10-phenanthroline, which could be generalized to account for emission of other similar hybrid systems.

1. Introduction

Zinc oxide low-dimensional nanostructures, such as nanowalls, nanobelts and nanorods, have recently attracted a lot of attention with ongoing research for applications in optoelectronics and photonic devices [1–10], because of the wide and direct band-gap and a large exciton binding energy (60 meV) of ZnO. The stability of the exciton makes ZnO a promising material for applications that take advantage of its band-gap emission. Furthermore, ZnO nanostructures excited by deep UV light produce photoluminescence (PL) emissions spanning over the UV and visible regions, which are associated with electron-hole recombination and various intrinsic defects. The spectral shapes and intensities of the near band-gap luminescence are found to greatly depend on the dimension and morphology of the nanostructure due to quantum confinement effect [11–13].

Recently, much attention has been paid to near-infrared (NIR) luminescence from trivalent lanthanide ions because of their applications in telecommunication, bioanalysis and solar cell [14–17]. However, ZnO nanostructures themselves have not been found to produce any emission in the NIR region. A few attempts have been conducted to realize NIR emission from ZnO nanostructures by doping rare earth (RE) ions [18–22]. Among the RE elements, Nd^{3+} and Er^{3+} are very attractive for generating NIR luminescence in nanophotonics because these two cations produce characteristic luminescence at wavelengths close to 1300 and 1500 nm, respectively [23,24]. For Er^{3+}-doped ZnO nanostructures, NIR emissions could be achieved by co-doping RE cations with neutral atoms and/or cations of another element into the ZnO lattice. For example, co-doping of N and Li into ZnO:Er^{3+} has been found to produce an effective NIR emission by modifying the local symmetry and structure around Er^{3+} [20–22]. The formation of silicon nanocrystals in the ZnO lattice has been reported to generate the 1.53 μm emission by energy transfer from the Si nanocrystals to Er^{3+} [25]. To date, however, no NIR emission has been generated from Nd^{3+}-doped ZnO nanostructures by the band-gap excitation (in the UV region). Liu et al. observed NIR luminescence of Nd^{3+}-doped ZnO nanocrystals in the 800–1500 nm range upon a 811-nm laser excitation [26]. We have previously fabricated Eu^{3+}-doped ZnO nanowalls on an ITO-glass substrate by a facile electrochemical method [10]. Although the doping of the Eu^{3+} ions has definitively been confirmed, both as-grown and thermally annealed ZnO:Eu^{3+} nanowalls excited by a 325-nm HeCd laser do not produce the characteristic red emission from the Eu^{3+} dopant. In contrast, surface modification of the sample by 1,10-phenanthroline (phen, $C_{12}H_8N_2$) has led to a sharp Eu^{3+} emission at 620 nm. We attribute the observed red emission from Eu^{3+} to a unique cascade energy transfer from ZnO to Eu^{3+} via phen, which plays a dual role both as an energy acceptor from ZnO and as an energy donor to the Eu^{3+} ion. Here, we investigate NIR luminescence generation by ZnO nanowalls via surface functionalization with other RE complexes, such as Nd^{3+} and Er^{3+} complexes bearing UV-absorbing ligands, in order to exploit the underlying energy transfer mechanism and their wide range of potential applications.

The present study is designed to investigate the nature and the

* Corresponding author at: Nanotechnology Research Centre, National Research Council of Canada, 11421 Saskatchewan Drive, Edmonton, AB T6G 2M9, Canada.
** Corresponding author.
E-mail addresses: Jung-Soo.Kang@nrc-cnrc.gc.ca (J.-S. Kang), tong@uwaterloo.ca (K.T. Leung).

https://doi.org/10.1016/j.apsusc.2019.144874
Received 26 July 2019; Received in revised form 16 November 2019; Accepted 25 November 2019
Available online 29 November 2019

luminescence properties of ZnO nanowalls surface-functionalized by RE^{3+} (RE = Nd and Er) complexes. Phen is selected as both the chelating ligand and energy-transfer mediator in the cascade energy transfer from ZnO to the RE^{3+} ions, because of its large π-conjugated system that could potentially enable a one-step mechanism for the cascade energy transfer from ZnO to REs for generating the NIR luminescence. The surfaces of as-grown and functionalized ZnO nanowalls are characterized by Raman and XPS spectroscopies, and the interfacial interactions between the adsorbed RE^{3+} phen complex and the ZnO surface are studied by using Hartree-Fock calculations. In addition, plausible energy transfer processes for the observed sensitized NIR luminescence due to the Nd^{3+} complex are proposed.

2. Experimental details

Synthesis of ZnO:Tb(III) Nanowalls and REPhen complexes. Zinc nitrate hexahydrate (≥98%), potassium chloride (≥99.0%), neodymium nitrate hexahydrate (99.9%), erbium nitrate pentahydrate (99.9%), 1,10-phenanthroline (≥99.0%) and methanol (≥99.9%) were purchased from Sigma-Aldrich and used without further purification. ZnO nanowalls were synthesized in an aqueous solution of 0.1 M Zn $(NO_3)_2{\cdot}6H_2O$ and 0.1 M KCl using a three-electrode electrochemical cell with an applied voltage of −1.3 V vs Ag/AgCl on the working electrode. ITO-coated glass was used as the substrate and the working electrode, with a Pt wire as the counter electrode and Ag/AgCl as the reference electrode. Deposition was carried out at a constant temperature of 70 °C maintained in a water bath. For the synthesis of REPhen complexes, the appropriate rare earth nitrate salt and 1,10-phenanthroline with the molar ratio of 1:8 were dissolved in methanol. The solution was then stirred for 12 h and filtered. The resulting solid complexes were rinsed with methanol and kept under vacuum.

Surface modification. The surface of ZnO nanowalls was treated separately by drop-casting an aliquot (10 μL) of the prepared two complexes, $Nd(phen)_2(NO_3)_3$ and $Er(phen)_2(NO_3)_3$, dissolved in ethylacetate (0.1 mM). These two surface-functionalized ZnO nanowalls are referred to as NdPhen/ZnO nanowalls and ErPhen/ZnO nanowalls. It should be noted that small amounts of these complexes deposited onto quartz slides (i.e. without any predeposited ZnO nanowalls) did not produce any NIR emission from the Nd complex by a 325-nm He-Cd laser.

Characterization. The morphologies of pristine and surface-functionalized ZnO nanowalls were investigated by field-emission scanning electron microscopy (SEM) in a Hitachi S-4800 microscope. The chemical nature of pristine Phen, NdPhen and NdPhen/ZnO nanowalls was analysed by X-ray photoelectron spectroscopy (XPS) in a Thermo-VG Scientific ESCALab 250 Microprobe equipped with a monochromatic Al Kα (1486.6 eV) X-ray source and a charge compensation capability. For PL measurement, the samples were excited by a 325 nm He-Cd laser and the spectra were collected by an ARC 0.5 m Czerny–Turner monochromator equipped with a cooled Hamamatsu R-933–14 photomultiplier tube. A Raman spectrophotometer (LabRAM HR-800, Horiba) with a 514.5 nm Ar^+ laser was employed to obtain the Raman spectra.

3. Results and discussion

Fig. 1 shows the SEM images of pristine and surface-functionalized nanowalls electrochemically deposited on ITO-coated glass. They appear to be vertically oriented and the ledge thickness of ZnO nanowalls is in the range of 50–200 nm. Evidently, surface functionalization using NdPhen shows minimal changes in the morphology and similar nanostructures remain after surface functionalization.

Raman spectra of ZnO nanowalls, NdPhen $[Nd(phen)_2(NO_3)_3]$ complexes (in powder form) and NdPhen/ZnO nanowalls are measured in the 100–4000 cm^{-1} range by using a 514.5-nm Ar ion laser (Fig. 2a). Evidently, characteristic bands for ZnO nanowalls are observed at 101, 211, 257, 397, 439, 554, 735, 911 and 1068 cm^{-1} in the low-wavenumber region (with an expanded view shown in Fig. 2a, right inset), and a triplet feature at 3490 cm^{-1} in the high-wavenumber region. Wurtzite ZnO with C_{6v}^4 symmetry has six optical modes corresponding to zone-center phonons represented as $\Gamma_{opt} = A_1 + 2B_1 + E_1 + 2E_2$. Both the A_1 and E_1 modes are each split into a transverse optical (TO) and a longitudinal optical (LO) components, and the two E_2 modes are specified as low (E_2^{low}) and high (E_2^{high}) frequency modes. The B_1 mode is principally inactive under the C_{6v}^4 symmetry in Raman spectroscopy. Based on the reported zone-center optical phonon frequencies, we summarize the assignments for the observed Raman peaks in Table S1 (Supporting Information). For most ZnO morphologies, including powders, bulk crystals, nanoparticles and nanorods, the intensity of the E_2 mode at 439 cm^{-1} is predominant [27–30]. However, the relative intensities between the A_1(LO) and the E_2^{high} modes are found to be greatly dependent on the measurement geometry [31]. As ZnO nanowalls electrochemically grown on an ITO substrate in an electrolyte containing Cl^- have the preferred growth direction of [1 0 $\bar{1}$ 0], this results in a large area of exposed [0 0 0 1] surface [32]. The relatively strong intensity found for the A_1(TO) feature, located at 397 cm^{-1}, indicates that Raman scattering from the [0 0 0 1] facet provides more contribution to the intensity than the [1 0 $\bar{1}$ 0] facet. In addition, while the acoustic phonon overtone associated with the A_1 mode at 331 cm^{-1} was reported in previous studies, they are not evident in ZnO nanowalls upon the 514.5 nm excitation [29,30]. Instead, the combinations of the acoustic A_1 overtones and the optical A_1(TO) mode at 735 and 911 cm^{-1} are observed. The presence of a strong band with triplet peaks (at 3458, 3490, 3567 cm^{-1}), which correspond to the OH vibrations, originates from $Zn(OH)_2$ that presents as an intermediate product in the ZnO electrochemical synthesis.

The Raman spectra for the NdPhen powder sample and the NdPhen/ZnO nanowalls are also shown in Fig. 2a. The Raman spectrum of NdPhen/ZnO nanowalls essentially contains all the spectral features of ZnO nanowalls and NdPhen powder, with several primary features characteristic of the adsorbed Nd^{3+} complex and ZnO nanowalls. Evidently, there is no significant change in the intensity of individual features originated from the ZnO nanowalls before and after deposition of the NdPhen complex, which indicates that the structure of ZnO nanowalls has not been affected upon adsorption of the complex. The two bands at 725 cm^{-1} (s) and 864 cm^{-1} (w) correspond to the out-of-plane motion of H atoms on the heterocycle and the center ring, respectively [33]. The next two bands at 1035 and 1297 cm^{-1} are assigned as ν_s(O—N—O) and ν_a(O—N—O) vibrations of the chelating bidentate nitrate ion, respectively [34]. Among the observed bands, only the symmetric stretching ν_s(O—N—O) mode, with two components at 1027 and 1035 cm^{-1}, exhibits structural change upon the adsorption and becomes broadened (Fig. 2a, left inset). This spectral change suggests that there is an interaction between the surface of ZnO nanowalls and adsorbed NdPhen. As the A_1 band of phen at 1031 cm^{-1} has been previously found to shift to 1050 cm^{-1} in surface enhanced Raman scattering, this leads us to assign the observed 1053 cm^{-1} feature to the A_1 mode of phen adsorbed on ZnO nanowalls [35].

To investigate the bonding nature between NdPhen and ZnO nanowalls, X-ray photoelectron spectroscopy (XPS) data have been obtained for phen, NdPhen and NdPhen/ZnO nanowalls, and they are compared in Fig. 2b and c. From the molecular structure of phen, two C 1 s peaks corresponding to the aromatic C—C bond and C—N bond are expected. Their respective C 1s peak positions, 285.8 and 286.5 eV, appear not affected by bonding to Nd or upon adsorption of NdPhen on the surface of ZnO nanowalls (Fig. 2b). On the other hand, N 1s peaks demonstrate the change in the chemical nature with and without adsorption on the ZnO nanowalls. The N 1s peak at 400.1 eV attributed to C—N bonding in NdPhen remains unchanged before and after the adsorption. In contrast, the N 1s peak at 407.6 eV corresponding to NO_3^- in NdPhen appears to shift to a lower binding energy (407.0 eV) upon adsorption on ZnO nanowalls. Together with the spectral changes

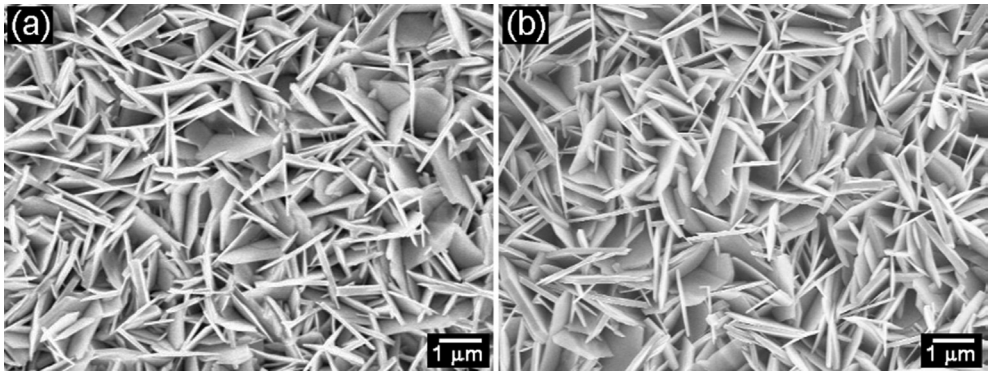

Fig. 1. SEM images of (a) pristine ZnO nanowalls and (b) NdPhen functionalized ZnO nanowalls.

observed in the Raman spectra, this confirms that bonding is established between the positively charged nitrogen atoms in the nitrate ions and the oxygen atoms nearby the surface of ZnO nanowalls.

In order to evaluate the interfacial nature of NdPhen/ZnO hybrid system, we perform ab-initio Hartree-Fock calculations using the GENECP basis set (MWB50 for Nd, 3-21G for Zn, O, C, N and H) in Gaussian 09 [36]. A $Zn_{29}O_{29}$ cluster consisting of four layers along the [0 0 0 1] direction is used to provide the facet with a minimum area sufficiently large to accommodate the Nd^{3+} complex, while the periodic boundary condition of ZnO is employed for the optimization. As shown in Fig. 3, we start the optimization calculation with two different initial configurations for the Nd complex-$Zn_{29}O_{29}$ hybrid system. The complex is placed with one of the O atoms in the terminal NO_3^- group approaching perpendicularly to the center of the Zn layer in Model I (face-on), and toward to the O atom array located at the vertices between [0 0 0 1] and [1 0 $\bar{1}$ 0] planes in Model II (edge-on). It should be noted that Model II is considered here to evaluate plausible adsorption configurations on the edges of very thin nanowalls. Since the $Zn_{29}O_{29}$ crystal structure is assumed not to be affected by the adsorption of the complex, the positions of all Zn and O atoms in ZnO has been fixed during the geometry optimization, while the complex is allowed to move and relax by long-range interactions (such as van der Waals or electrostatic forces). The calculations show similar trends as our experimental results. In particular, the average atomic charge value of the N atoms in the nitrate groups decreases from 0.696 before the adsorption to 0.631 after the adsorption. The separations between NdPhen and ZnO in both models become smaller after geometry optimization, which is most likely due to the interfacial interaction between ZnO and one of the NO_3 groups in NdPhen. In effect, one of the nitrate ion groups in NdPhen acts as an anchor and tows along the remaining bulky $Nd(NO_3)_2(phen)_2$ moiety. The strong electrostatic interactions

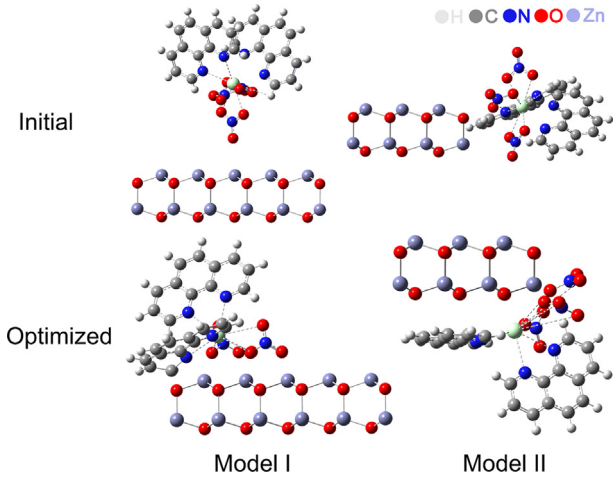

Fig. 3. Optimized equilibrium geometries for NdPhen/$Zn_{29}O_{29}$ obtained from two initial configurations: the NdPhen placed with its NO_3 group perpendicular to the Zn layer (face-on, model I) and toward the oxygen layer at the edge between [0 0 0 1] and [1 0 $\bar{1}$ 0] facets (edge-on, model II).

between Zn in the $Zn_{29}O_{29}$ cluster and an O atom in the nitrate groups induce repositioning one of the two phen moieties (hereafter, referred to as phen-1) parallel to the Zn surface layer for Model I, and to the O surface layer for Model II. As a result, the other phen moiety (denoted here as phen-2) is moved to the perpendicular position to the Zn layer in Model I and to the O layer in Model II. We further calculate the binding energy E_b of the NdPhen/ZnO hybrid system as follows [37]:

$$E_b = E_{\mathrm{NdPhen/ZnO}} - (E_{\mathrm{ZnO}} + E_{\mathrm{NdPhen}})$$

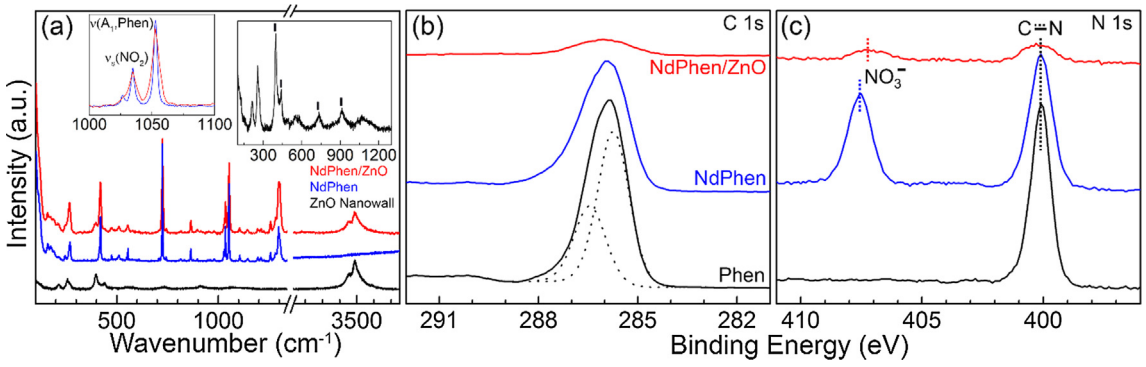

Fig. 2. (a) Raman spectra of ZnO nanowalls (bottom), NdPhen powder (center) and NdPhen/ZnO hybrid nanostructures (top). Left inset displays a spectral comparison of NdPhen and NdPhen/ZnO hybrid nanostructures over an expanded scale of 1000–1100 cm^{-1} and right inset shows an expanded view of 100–1300 cm^{-1} for ZnO nanowalls. The black markers in the right inset indicate the peaks discussed in the main text. XPS spectra of (b) C 1s and (c) N 1s regions of phen powder, NdPhen powder and NdPhen/ZnO hybrid nanostructures.

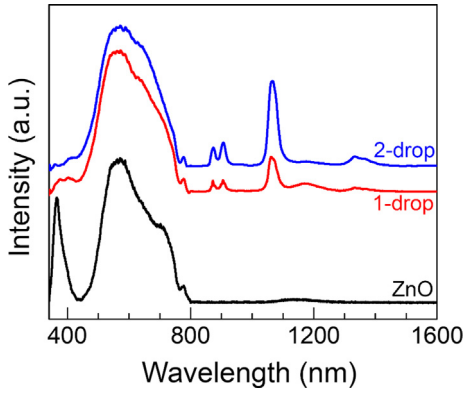

Fig. 4. PL spectra (λ_{exn} = 325 nm) of pristine ZnO nanowalls, and upon casting of 1-drop and 2-drop NdPhen complex.

where $E_{NdPhen/ZnO}$ is the total energy for the equilibrium structure of the NdPhen/ZnO hybrid system, and E_{ZnO} and E_{NdPhen} are the total energies of the equilibrium structures of the ZnO cluster and the NdPhen complex, respectively. With the difference between the calculated binding energies for Model I (17.008 eV/molecule) and Model II (17.004 eV/molecule) to be 4 meV, these results indicate that both bonding geometries are plausible.

To observe the influence of surface functionalization, PL spectra of the as-grown ZnO nanowalls and NdPhen/ZnO nanowalls are measured at room temperature in the near-UV to near-IR region and they are shown in Fig. 4. Upon excitation by a 325-nm He-Cd laser, the as-grown ZnO nanowalls produce a near band-gap (NBG) emission at 365 nm with a narrow bandwidth and a broad deep-level emission band spanning over the 440–800 nm range. Drop-casting of one drop of the NdPhen complex solution produces NdPhen/ZnO nanowalls with the characteristic NIR emission originated from Nd^{3+}, as well as the NBG and deep-level emissions (Fig. 4). The three bands barycentered at 887, 1066 and 1334 nm were associated with the $^4F_{3/2} \rightarrow {}^4I_J$ (J = 9/2, 11/2 and 13/2) transitions, respectively. Among them, the $^4F_{3/2} \rightarrow {}^4I_{11/2}$ transition gives the strongest emission intensity. Upon casting with one additional drop, the intensities of these spectral features increase by more than two-fold (Fig. 4). The NdPhen in NdPhen/ZnO hybrid structure is also found to have a significant effect on the NBG emission from the ZnO nanowalls. As the ZnO nanowalls are surface-modified by the NdPhen complex, the NBG emission has dramatically decreased in intensity and it appears as a trace after the 2-drop treatment. Interestingly, the spectral feature of the deep-level emission remains essentially unchanged. We attribute this unexpected spectral evolution to the spectral overlap between the NBG emission and the excitation of phen, which triggers an energy transfer process. In the case of ErPhen/ZnO nanowalls, the reduction of the NBG emission is observed due to the energy transfer to phen, similar to the NdPhen/ZnO system. No NIR emission is, however, found for the ErPhen/ZnO nanowall structures. This result therefore suggests that the transferred energy to phen is predominantly dismissed by non-radiative processes for ErPhen/ZnO nanowalls. In the previously reported case of ZnO:Eu^{3+} nanowalls surface-functionalized by phen, the phen molecule is linked to the Zn and Eu atoms through its two N atoms. In this case, the cascade energy transfer takes place from ZnO to Eu^{3+} through those bonds [10]. The Dexter electron-exchange process is attributed to the cascade energy transfer because the distances of the donor-acceptor pairs are sufficiently small to facilitate orbital overlap [38]. In the present case of NdPhen/ZnO nanowalls, a NIR luminescence observed in the excited NdPhen/ZnO nanowalls is also expected to follow a similar cascade energy transfer mechanism via two steps. However, the energy transfer mechanism for NdPhen/ZnO nanowalls is different from the case for phen surface-functionalized ZnO:Eu^{3+} (as discussed below). For the NdPhen/ZnO nanowalls, the first step corresponds to the energy

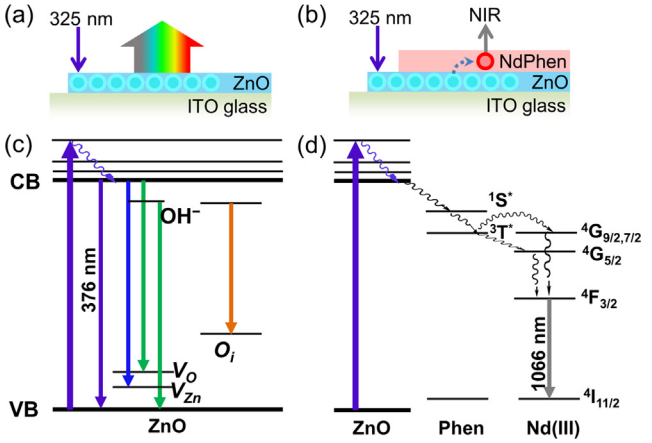

Fig. 5. Schematic model of radiative relaxation occurring in (a) ZnO and (b) NdPhen/ZnO hybrid structures. Corresponding energy-level diagrams for (c) ZnO and (d) cascade energy transfer from ZnO to Nd^{3+} via phen.

transfer between electronically independent donor (ZnO) and acceptor (phen) components, while the second step involves the intramolecular energy transfer from phen to Nd^{3+}.

Fig. 5 shows a schematic model illustrating the cascade energy transfer mechanism for NdPhen/ZnO nanowall structures. The Coulombic interaction between the donor ZnO nanowalls and the acceptor phen moieties enables the first step of the cascade energy transfer, which can be explained by the Förster resonant energy transfer (FRET) mechanism. Since the interfacial interaction between the nitrate anions in the NdPhen complex, which only act as anchors, and the surface of the ZnO nanowalls causes phen to be in sufficiently close proximity to the underlying ZnO nanowalls, as shown in Fig. 3. As a consequence, this close proximity enables highly efficient FRET from NBG of ZnO nanowalls to phen. The energy transfer efficiency Q_{ET} from the ZnO nanowalls to the NdPhen complex can be evaluated using the following relation [39]:

$$Q_{ET} = \left(1 - \frac{A_{NdPhen/ZnO}}{A_{ZnO}}\right)$$

where $A_{NdPhen/ZnO}$ and A_{ZnO} are the integrals of the PL spectra (NBG and defect emissions) of the NdPhen/ZnO nanowalls and the ZnO nanowalls, respectively. Applying the integral to the entire spectrum range, the energy transfer efficiency $Q_{ET}^{Overall}$ for ZnO nanowalls after 1-drop and 2-drop treatments of NdPhen are 0.10 and 0.11, respectively. The FRET process is usually quantified by the Förster radius, R_0, defined as the distance between the energy acceptor and donor at which the energy transfer efficiency is 50%. Introducing the acceptor/donor ratio (r) within the optically observed cross-section to the Förster model for this complex interaction, Q_{ET} can be expressed in terms of R_0 and the distance between the energy donor and acceptor, d, as [40]:

$$Q_{ET} = \frac{rR_0^6}{rR_0^6 + d^6}$$

When r = 1, the energy corresponding to the NBG emission is totally transferred to phen and Q_{ET} becomes the maximum 0.11. Assuming that two different phen moieties (phen-1 and phen-2) are involved in the FRET processes, Q_{ET} = Q_{ET} (phen-1) + Q_{ET} (phen-2). Taking d as an average value of the N-to-Zn separations between two N atoms and Zn atoms from the optimized geometry, d = 3.2 Å for phen-1 and d = 6.8 Å for phen-2, we obtain R_0 = 2.3 Å, and Q_{ET} (phen-2) is only 1.3 × 10^{-3}. For NdPhen/ZnO nanowalls, the Förster distance between the donor ZnO nanowalls and the acceptor phen is exceptionally small, when compared with typical values in the range of 1 – 10 nm. This is due to the strong electrostatic interaction between the ZnO layers and nitrate anions that leads to the phen-1 moiety being

close to the ZnO surface.

The energy transfer for the second step begins with the intersystem crossing between the $^1\pi\pi^*$ and the $^3\pi\pi^*$ states of phen, followed by the intramolecular energy transfer from phen to Nd^{3+}. The energy-transfer rate from the triplet-excited state of phen to the rare-earth ion in the solid has been well elucidated from exchange-interaction theory [38]. The exchange interaction is active if the emission band of a sensitizer (S) overlaps the 4f–4f absorption band of the lanthanide ion. As shown in Fig. S1, some absorption bands of Nd^{3+} and Er^{3+} nicely overlap with the phosphorescence band of phen. The second energy transfer promotes the $^4I_{9/2} \rightarrow {}^4G_J$ (J = 5/2, 7/2 and 9/2) transitions of Nd^{3+} and the $^4I_{15/2} \rightarrow {}^2H_{11/2}$ and $^4F_{7/2}$ transitions of Er^{3+}. Among the electronic transitions from the ground states in the UV – visible range, the $^4I_{9/2} \rightarrow {}^4G_{5/2}$ transition (at 574.8 nm) for Nd^{3+} and the $^4I_{15/2} \rightarrow {}^2H_{11/2}$ transition (at 523.0 nm) for Er^{3+} are most hypersensitive [41]. The overlapping with the hypersensitive absorption bands of the acceptor maximizes the energy transfer efficiency. A model for the energy transfer processes from the triplet spin state of phen to the electronic states of RE^{3+} as the receiving levels is shown in Fig. S2. The cascade energy transfer rates from ZnO nanowalls to Nd^{3+} and Er^{3+} via the intercessor phen are expected to be very similar to each other, because of the similarities in the adsorption configurations and the spectral overlaps (Fig. S1). The difference in the energy transfer processes between Nd^{3+} and Er^{3+} is in the intramolecular energy transfer from the receiving levels to the emitting levels. The energy gap (ΔE) between the main receiving $^2H_{11/2}$ level and the emitting $^4I_{13/2}$ level of Er^{3+} is 12,600 cm^{-1}, which is much larger than ΔE = 5850 cm^{-1} ($^4G_{5/2} \rightarrow {}^4F_{3/2}$) and 5950 cm^{-1} ($^4G_{7/2} \rightarrow {}^4F_{3/2}$) for Nd^{3+}. This relatively large energy gap of Er^{3+} causes non-radiative relaxation process in ErPhen/ZnO hybrid structure and prevents generation of NIR emission.

4. Conclusion

In summary, we present the first observation of sensitized NIR emission from hybrid NdPhen complex/ZnO nanowalls via the cascade energy transfer from the NBG emission of ZnO nanowalls to Nd^{3+} via phen. Optimized geometries of NdPhen on model ZnO clusters obtained by ab-initio calculations along with XPS results support plausible interfacial interaction between the nitrate anions in NdPhen and the surface of ZnO nanowalls. In addition, phen appears to play a key role as an energy mediator, i.e., an acceptor from ZnO nanowalls and a donor to Nd^{3+}. Although the surface of ZnO nanowalls is treated only by drop-casting a dilute solution of the NdPhen complex, the intensity of the NIR from NdPhen/ZnO nanowalls is as strong as that of the complex powder due to transferred energy from ZnO NBG emission. In contrast, the absence of any sensitized NIR emission from hybrid ErPhen/ZnO nanowalls is due to the large energy gap between the receiving and the emitting levels of Er^{3+}. The present work provides strong evidence for the cascade energy transfer mechanism resulting from the surface modification of ZnO nanowalls. NdPhen functionalization therefore offers an effective route for exploiting the application of photophysical properties of ZnO nanowalls to a wide spectral range from near-UV to the NIR. We also believe that this cascade energy transfer mechanism can be generalized to other organic complex/semiconducting metal oxide hybrid structures that promise new NIR-wavelength optoelectronics and other applications.

Declaration of Competing Interest

The authors declare that they have no known competing financial interests or personal relationships that could have appeared to influence the work reported in this paper.

Acknowledgment

This work was supported by the Natural Sciences and Engineering Research Council of Canada.

Appendix A. Supplementary material

Supplementary data to this article can be found online at https://doi.org/10.1016/j.apsusc.2019.144874.

References

[1] A.B. Djurišić, A.M.C. Ng, X.Y. Chen, ZnO nanostructures for optoelectronics: material properties and device applications, Prog. Quant. Electron. 34 (2010) 191–259, https://doi.org/10.1016/j.pquantelec.2010.04.001.
[2] R. Araneo, A. Rinaldi, A. Notargiacomo, F. Bini, M. Pea, S. Celozzi, F. Marinozzi, G. Lovat, Design concepts, fabrication and advanced characterization methods of innovative piezoelectric sensors based on ZnO nanowires, Sensors 14 (2014) 23539–23562, https://doi.org/10.3390/s141223539.
[3] M.H. Asif, B. Danielsson, M. Willander, ZnO nanostructure-based intracellular sensor, Sensors 15 (2015) (1804) 11787–11804, https://doi.org/10.3390/s150511787.
[4] Y. Ning, Z. Zhang, F. Teng, X. Fang, Novel transparent and self-powered UV photodetector based on crossed ZnO nanofiber array homojunction, Small 14 (2018) 1703754, https://doi.org/10.1002/smll.201703754.
[5] S. Liu, M.-Y. Li, D. Su, M. Yu, H. Kan, H. Liu, X. Wang, S. Jiang, Broad-band high-sensitivity ZnO colloidal quantum dots/self-assembled Au nanoantennas heterostructures photodetectors, ACS Appl. Mater. Interfaces 10 (2018) 32516–32525, https://doi.org/10.1021/acsami.8b09442.
[6] D. Xiong, W. Deng, G. Tian, Y. Gao, X. Chu, C. Yan, L. Jin, Y. Su, W. Yan, W.A. Yang, Piezo-phototronic enhanced serrate-structured ZnO-based heterojunction photodetector for optical communication, Nanoscale 11 (2019) 3021–3027, https://doi.org/10.1039/C8NR09418G.
[7] F.R. Fan, W. Tang, Z.L. Wang, Flexible nanogenerators for energy harvesting and self-powered electronics, Adv. Mater. 28 (2016) 4283–4305, https://doi.org/10.1002/adma.201504299.
[8] R.M. Hewlett, M.A. McLachlan, Surface structure modification of ZnO and the impact on electronic properties, Adv. Mater. 28 (2016) 3893–3921, https://doi.org/10.1002/adma.201503404.
[9] J.-S. Kang, A.-R. Ham, J.-G. Kang, K.T. Leung, White and tunable emission from and rhodamine B detection by modified zinc oxide nanowalls, Langmuir 34 (2018) 9774–9780, https://doi.org/10.1021/acs.langmuir.8b01238.
[10] J.-S. Kang, Y.-K. Jeong, J.-G. Kang, L. Zhao, Y. Sohn, D. Pradhan, K.T. Leung, Observation of mediated cascade energy transfer in europium-doped ZnO nanowalls by 1,10-phenanthroline, J. Phys. Chem. C 119 (2015) 2142–2147, https://doi.org/10.1021/jp5090795.
[11] C.H. Ahn, Y.Y. Kim, D.C. Kim, S.K. Mohanta, H.K. Cho, A Comparative analysis of deep level emission in ZnO layers deposited by various methods, J. Appl. Phys. 105 (2009) 013502, https://doi.org/10.1063/1.3054175.
[12] J. Fan, F. Güell, C. Fábrega, A. Fairbrother, T. Andreu, A.M. López, J.R. Morante, A. Cabot, Visible photoluminescence components of solution-grown ZnO nanowires: influence of the surface depletion layer, J. Phys. Chem. C 116 (2012) 19496–19502, https://doi.org/10.1021/jp302443n.
[13] K.H. Tam, C.K. Cheung, Y.H. Leung, A.B. Djurišić, C.C. Ling, C.D. Beling, S. Fung, W.M. Kwok, W.K. Chan, D.L. Phillips, L. Ding, W.K. Ge, Defects in ZnO nanorods prepared by a hydrothermal method, J. Phys. Chem. B 110 (2006) 20865–20871, https://doi.org/10.1021/jp063239w.
[14] G. Chen, C. Yang, P.N. Prasad, Nanophotonics and nanochemistry: controlling the excitation dynamics for frequency up- and down-conversion in lanthanide-doped nanoparticles, Acc. Chem. Res. 46 (2013) 1474–1486, https://doi.org/10.1021/ar300270y.
[15] T. Zhong, J.M. Kindem, E. Miyazono, A. Faraon, Nanophotonic coherent light–matter interfaces based on rare-earth-doped crystals, Nat. Commun. 6 (2015) 8206, https://doi.org/10.1038/ncomms9206.
[16] I. Martinić, S.V. Eliseeva, S. Petoud, Near-infrared emitting probes for biological imaging: organic fluorophores, quantum dots, fluorescent proteins, lanthanide(III) complexes and nanomaterials, J. Lumin. 189 (2017) 19–43, https://doi.org/10.1016/j.jlumin.2016.09.058.
[17] G. Bai, Z. Yang, H. Lin, W. Jie, J. Hao, Lanthanide Yb/Er Co-doped semiconductor layered WSe_2 nanosheets with near-infrared luminescence at telecommunication wavelengths, Nanoscale 10 (2018) 9261–9267, https://doi.org/10.1039/C8NR01139G.
[18] S. Ji, L. Yin, G. Liu, L. Zhang, C. Ye, Synthesis of rare earth ions-doped ZnO nanostructures with efficient host – guest energy transfer, J. Phys. Chem. C 113 (2009) 16439–16444, https://doi.org/10.1021/jp906501n.
[19] L.-C. Chao, J.-W. Huang, C.-W. Chang, Annealing effects on the properties of Nd containing ZnO nanoparticles prepared by sol–gel process, Physica B 404 (2009) 1301–1304, https://doi.org/10.1016/j.physb.2008.12.013.
[20] F. Pavón, A. Urbieta, P. Fernández, Luminescence and light guiding properties of Er and Li codoped ZnO nanostructures, J. Lumin. 195 (2018) 396–401, https://doi.org/10.1016/j.jlumin.2017.11.059.
[21] Z. Zhou, T. Komori, T. Ayukawa, A. Koizumi, N. Matsunami, Y. Takeda, M. Morinaga, Doping effects on 1.54 μm photoluminescence from Er-containing ZnO, Opt. Mater. 28 (2006) 727–730, https://doi.org/10.1016/j.optmat.2005.09.006.
[22] J.-W. Lo, W.-C. Lien, C.-A. Lin, J.-H. He, Er-doped ZnO nanorod arrays with

enhanced 1540 nm emission by employing Ag island films and high-temperature annealing, ACS Appl. Mater. Interfaces 3 (2011) 1009–1014, https://doi.org/10.1021/am101031f.
[23] W.T. Carnall, P.R. Fields, K. Rajnak, Electronic energy levels in the Trivalent Lanthanide Aquo Ions. I. Pr^{3+}, Nd^{3+}, Pm^{3+}, Sm^{3+}, Dy^{3+}, Ho^{3+}, Er^{3+}, and Tm^{3+}, J. Chem. Phys. 49 (1968) 4424–4442, https://doi.org/10.1063/1.1669893.
[24] J.-S. Kang, K.T. Leung, M.-K. Nah, J.-S. Shin, M.-H. Kang, B. Shong, J.-G. Kang, J. Lee, Y. Sohn, Neighbour-sensitized near-infrared emission of New Nd(III) and Er (III) complexes with 1-(anthracene-2-yl)-4,4,4-trifluoro-1,3-butanedione, New J. Chem. 40 (2016) 9702–9710, https://doi.org/10.1039/C6NJ00999A.
[25] Y. Pu, F. Xu, Z. Jiang, Z. Ma, F. Lu, D. Chen, Enhanced broadband emission from Er-Tm codoped ZnO film due to energy transfer processes involving Si nanocrystals, Appl. Phys. Lett. 101 (2012) 191903, https://doi.org/10.1063/1.4766348.
[26] Y. Liu, W. Luo, R. Li, H. Zhu, X. Chen, Near-infrared luminescence of Nd^{3+} and Tm^{3+} ions doped ZnO nanocrystals, Opt. Express 17 (2009) 9748–9753, https://doi.org/10.1364/OE.17.009748.
[27] R. Zhang, P.-G. Yin, N. Wang, L. Guo, Photoluminescence and Raman scattering of ZnO nanorods, Solid State Sci. 11 (2009) 865–869, https://doi.org/10.1016/j.solidstatesciences.2008.10.016.
[28] F. Decremps, J. Pellicer-Porres, A.M. Saitta, J.-C. Chervin, A. Polian, High-pressure Raman spectroscopy study of wurtzite ZnO, Phys. Rev. B 65 (2002) 092101, https://doi.org/10.1103/PhysRevB.65.092101.
[29] M. Rajalakshmi, A.K. Arora, B.S. Bendre, S. Mahamuni, Optical phonon confinement in zinc oxide nanoparticles, J. Appl. Phys. 87 (2000) 2445–2448, https://doi.org/10.1063/1.372199.
[30] K.J. Chen, T.H. Fang, F.Y. Hung, L.W. Ji, S.J. Chang, S.J. Young, Y.J. Hsiao, The crystallization and physical properties of Al-doped ZnO nanoparticles, Appl. Surf. Sci. 254 (2008) 5791–5795, https://doi.org/10.1016/j.apsusc.2008.03.080.
[31] N. Ashkenov, B.N. Mbenkum, C. Bundesmann, V. Riede, M. Lorenz, D. Spemann, E.M. Kaidashev, A. Kasic, M. Schubert, M. Grundmann, Infrared dielectric functions and phonon modes of high-quality ZnO films, J. Appl. Phys. 93 (2003) 126–133, https://doi.org/10.1063/1.1526935.
[32] D. Pradhan, K.T. Leung, Controlled growth of two-dimensional and one-dimensional ZnO nanostructures on indium tin oxide coated glass by direct electrodeposition, Langmuir 24 (2008) 9707–9716, https://doi.org/10.1021/la8008943.
[33] A.A. Schilt, R.C. Taylor, Infra-red spectra of 1: 10-phenanthroline metal complexes in the Rock Salt Region below 2000 cm^{-1}, J. Inorg. Nucl. Chem. (1959) 211–221, https://doi.org/10.1016/0022-1902(59)80224-4.
[34] W. Radecka-Paryzek, The template synthesis and characterization of hexaaza 18-membered macrocyclic complexes of cerium(III), praseodymium(III) and neodymium(III) nitrates, Inorg. Chim. Acta 109 (1985) L21–L23, https://doi.org/10.1016/S0020-1693(00)81760-0.
[35] Y. Peng, Z. Niu, W. Huang, S. Chen, Z. Li, Surface-enhanced Raman scattering studies of 1,10-phenanthroline adsorption and its surface complexes on a gold electrode, J. Phys. Chem. B 109 (2005) 10880–10885, https://doi.org/10.1021/jp0443198.
[36] M.J. Frisch, G.W. Trucks, H.B. Schlegel, G.E. Scuseria, M.A. Robb, J.R. Cheeseman, G. Scalmani, V. Barone, G.A. Petersson, H. Nakatsuji, X. Li, M. Caricato, A. Marenich, J. Bloino, B.G. Janesko, R. Gomperts, B. Mennucci, H.P. Hratchian, J.V. Ortiz, A.F. Izmaylov, J.L. Sonnenberg, D. Williams-Young, F. Ding, F. Lipparini, F. Egidi, J. Goings, B. Peng, A. Petrone, T. Henderson, D. Ranasinghe, V.G. Zakrzewski, J. Gao, N. Rega, G. Zheng, W. Liang, M. Hada, M. Ehara, K. Toyota, R. Fukuda, J. Hasegawa, M. Ishida, T. Nakajima, Y. Honda, O. Kitao, H. Nakai, T. Vreven, K. Throssell, J.A. Montgomery Jr., J.E. Peralta, F. Ogliaro, M. Bearpark, J.J. Heyd, E. Brothers, K.N. Kudin, V.N. Staroverov, T. Keith, R. Kobayashi, J. Normand, K. Raghavachari, A. Rendell, J.C. Burant, S.S. Iyengar, J. Tomasi, M. Cossi, J.M. Millam, M. Klene, C. Adamo, R. Cammi, J.W. Ochterski, R.L. Martin, K. Morokuma, O. Farkas, J.B. Foresman, D.J. Fox, Gaussian 09, Revision A.02, Gaussian Inc., Wallingford CT, 2016.
[37] M.J.S. Spencer, Gas sensing applications of 1D-nanostructured zinc oxide: insights from density functional theory calculations, Prog. Mater. Sci. 57 (2012) 437–486, https://doi.org/10.1016/j.pmatsci.2011.06.001.
[38] D.L. Dexter, A theory of sensitized luminescence in solids, J. Chem. Phys. 21 (1953) 836–850, https://doi.org/10.1063/1.1699044.
[39] T. Förster, Zwischenmolekulare Energiewanderung und Fluoreszenz, Ann. Phys. (Berlin) 437 (1948) 55–75, https://doi.org/10.1002/andp.19484370105.
[40] J.R. Lakowicz, Principles of Fluorescence Spectroscopy, second ed., Kluwer Academic, New York, 1999.
[41] R. Reisfeld, C.K. Jørgensen, Lasers and Excited States of Rare Earths, Springer-Verlag, Berlin/Heidelberg/New York, 1977 (Chapters 3, 7).